

Super Resolution for Root Imaging¹

Jose F. Ruiz-Munoz,² Alina Zare,^{2,3} Jyothier K. Nimmagadda,⁴ Shuang Cui,⁴ and James E.

Bacia⁴

² University of Florida, Department of Electrical and Computer Engineering, Gainesville, FL, USA

⁴ University of Florida, Department of Material Sciences and Engineering, Gainesville, FL, USA

Email addresses: JFR: jruizmunoz@ufl.edu

AZ: azare@ece.ufl.edu

JKN: jyothir@ufl.edu

SC: cuishuang413@ufl.edu

JEB: jebaciak@mse.ufl.edu

Number of words: 4880

ABSTRACT

- *Premise of the study:* High-resolution cameras have become very helpful for plant phenotyping by providing a mechanism for tasks such as target versus background discrimination, and the measurement and analysis of fine-above-ground plant attributes, e.g., the venation network of leaves. However, the acquisition of high-resolution (HR) imagery of roots in situ remains a challenge.
- *Methods:* We apply super-resolution (SR) convolutional neural networks (CNNs) to boost the resolution capability of a backscatter X-ray system designed to image buried roots. To overcome limited available backscatter X-ray data for training, we compare three alternatives for training: i) non-plant-root images, ii) plant-root images, and iii) pretraining the model with non-plant-root images and fine-tuning with plant-root images and two deep learning approaches i) Fast Super Resolution Convolutional Neural

¹ Manuscript received _____; revision accepted _____.

³ Author for correspondence: azare@ece.ufl.edu

Network and ii) Super Resolution Generative Adversarial Network). We evaluate SR performance using signal to noise ratio (SNR) and intersection over union (IoU) metrics when segmenting the SR images.

- *Results:* In our experiments, we observe that the studied SR models improve the quality of the low-resolution images (LR) of plant roots of an unseen dataset in terms of SNR. Likewise, we demonstrate that SR pre-processing boosts the performance of a machine learning system trained to separate plant roots from their background. In addition, we show examples of backscatter X-ray images upscaled by using the SR model.
- *Discussion:* The current technology for non-intrusive root imaging acquires noisy and LR images. In this study, we show that this issue can be tackled by the incorporation of a deep-learning based SR model in the image formation process.

Key words: Convolutional neural networks; generative adversarial networks; plant phenotyping; root phenotyping; super-resolution; backscatter X-ray. *[List 3 to 6 key words here in alphabetical order, separated by semicolons.]*

INTRODUCTION

In the last decade, advances in sensing devices and computer systems have allowed for the proliferation of high-throughput plant phenotyping systems (Das Choudhury et al. 2019). These systems are designed to acquire and analyze a large number of plant traits (Krieger 2014). However, the characterization of plant roots is challenging since they are “hidden” in the soil (Atkinson et al. 2019). We categorize the methods that have been used for root analysis as follows: **i) Non-imaging based in-situ methods:** these methods estimate traits of the root system architecture (RSA) by their correlations with chemical or physical properties. For example, in (Cseresnyés et al. 2018; Dalton 1995), the plant root electrical capacitance is used to estimate the root mass (the RSA is modeled as a resistance-capacitance circuit), likewise in (Cao et al. 2011), the electrical impedance spectroscopy (EIS)

approach is employed to model the RSA based on the frequency response. The disadvantage of these methods is that they do not provide morphological details since they are a simplified description of the RSA. **ii) Destructive methods:** in this category, we include the techniques that destroy the RSA during or after the imaging process. The most basic of this type is the one called “shovelomics” that consists of washing out the roots of the soil (Trachsel et al. 2011). Shovelomics can be applied in any type of soil, in contrast with other root phenotyping techniques that have limitations regarding the physical properties of the environment. However, it is not ideal for high-throughput because the manual excavation of the roots is labor-intensive and tedious. Also, most of the thin roots are missed in this process. **iii) Imaging under controlled conditions:** roots can be observed using rhizotrons, that are structures with windows that contain the soil where the plants are grown (Taylor et al. 1990). Also, 3-D imaging of RSA can be carried out by using special substrates, e.g., transparent substrates or easy-to-remove types of soil (Clark et al. 2011). These procedures allow acquiring high-quality images, but their main disadvantage is that the imaging acquisition is not made in situ. Therefore, the knowledge that can be inferred by them is limited. **iv) Intrusive methods:** this category encompasses the techniques where the acquisition device is introduced into the ground. We consider as intrusive methods the minirhizotrons that use a camera fixed into the soil through a tube to record sequences of pictures of parts of the RSA (Johnson et al. 2001), as well as soil coring (Wu et al. 2018). Although these methods do not necessarily result in the destruction of the RSA, they disturb the roots and soil, which might affect the natural root-soil interactions (Kolb et al. 2017). The disturbance can be worse when the devices are introduced and extracted frequently or when they are installed in stony soils (Majdi 1996). **v) Non-intrusive methods:** these techniques aim to image the RSA in situ, without disturbing the roots or the soil. In (Barton and Montagu 2004), ground-penetrating radar (GPR) technology was tested for this purpose ---it was possible to detect tree roots of 1 cm diameter buried in soil at 50 cm depth. However, GPR is currently limited to the detection of roots of trees or woody plants (Araus and Cairns 2014; Hirano et al. 2009). X-ray computerized tomography (CT) (Tabb et al. 2018) and magnetic resonance imaging (MRI) (Pflugfelder et al.

2017) ---that consist of scanning by devices traditionally used for medical applications--- can be grouped into this category when the complete plant can be scanned in the device (e.g., plants grown in pots). On the other hand, X-ray CT and MRI based analysis are intrusive when scanning extracted and washed RSA or soil-cores for root architectures removed from the field.

High-resolution sensors facilitate phenotyping by providing a mechanism for tasks such as target versus background discrimination (Han et al. 2014) or the measurement and analysis of small structures of the plants such as the venation network of leaves (Green et al. 2014; Endler 1998). As mentioned above, the acquisition of high-resolution (HR) imagery of roots in the field by non-intrusive methods remains a challenge. Therefore, an effective super-resolution (SR) algorithm that complements the image formation process ---by inferring HR details not clearly delineated by the sensing device--- is desired for the deployment of these systems in real-world applications.

The SR problem consists of estimating HR images from low-resolution (LR) images. SR has been used to overcome hardware limitations in applications that heavily rely on high-quality images, such as medical diagnosis (Zhang et al. 2012; Zhang and An 2017). Many SR methods in the literature use mathematical transformations of the original data to learn the LR to HR mapping (Yang et al. 2010; Zeyde et al. 2012). For instance, methods based on sparse representations reconstruct each image by a weighted combination of *words* from a set of basic patterns ---called a *dictionary*. A pair of LR-HR dictionaries are estimated from the LR-HR training data. A SR image is obtained by replacing the LR dictionary "words" by HR dictionary "words." Recently data-driven SR models based on deep-learning algorithms with convolutional neural networks (CNN) have become more popular than the sparse representation-based models. The SR deep-learning algorithms are preferred in many cases because they generally exhibit a better performance, as well as they can be applied as a "black box" when enough training data is available (Wang et al. 2015; Ledig et al. 2017). Particularly, super-resolution generative adversarial networks (SRGANs) have shown a high performance on the estimation of HR details loss in a degradation process (Ledig et al. 2017). However,

the implementation of a SR deep-learning model for root imagery is challenging because the large amount of HR and LR pairs needed for training are usually not available for technology in development. Additionally, an effective SR performance measure is unclear since it has been observed in previous studies that the reconstruction accuracy (pixel by pixel comparison of a HR-SR pair) and the perceptual quality (comparison of visual features of a HR-SR pair) are not directly correlated (Blau et al. 2019).

To enhance plant root imagery, we adapt two state-of-the-art deep learning approaches, the Fast Super-Resolution Convolutional Neural Network (FSRCNN) proposed in (Dong et al. 2016), and the Super Resolution Generative Adversarial Network (SRGAN). We train the SR models with LR-HR data of two non-root datasets (DIV2K and 91-image) and three plant root datasets (*Arabidopsis thaliana*, Wheat and Barley). These datasets were selected since they have considerable differences in textures and shapes, which encourage the model to find a general solution. Also, in order to facilitate the training of the generator, we introduce a modification of the SRGAN by implementing multiple discriminators (one discriminator per dataset). In the loss function, we consider the mean square error between HR-LR (that reduces the reconstruction error since it is low if the pixel values are similar), and the adversarial loss (that encourages the network to learn to add HR details to the LR image). To evaluate the SR performance, we use two methods: i) computing the standard signal to noise ratio (SNR) between the SR image and the original HR image; and ii) computing the intersection over union (IoU) when applying the SegRoot network (Wang et al. 2019) that detects plant roots on the images. We apply the SR model on images acquired by a prototype backscatter X-ray system.

The remainder of this paper is divided as follows. In Methods, we describe the backscatter X-ray system specs and the models used for training and testing the SR algorithms. In Results, we report the performance of the SR models. In Conclusion, we explain the relevant findings in our study and provide recommendations for the implementation of SR algorithms for root imaging.

METHODS

We apply machine-learning based techniques to boost the resolution capability of a backscatter X-ray system designed to image buried roots. In this section, we initially describe the characteristics of the backscatter X-ray system for imaging buried roots. Afterwards, we explain the mathematical background of the SR method and the settings that we use to train and test the SR models.

Backscatter X-ray radiography data

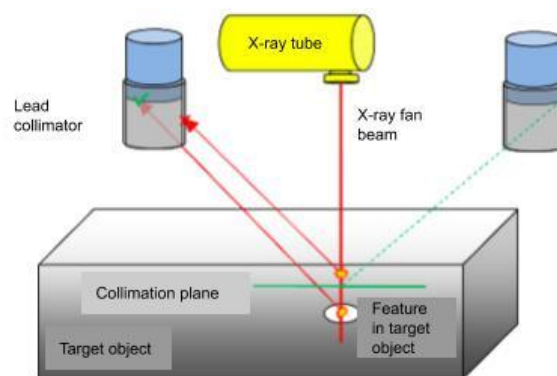


Figure 1. Single-sided backscatter X-ray technology for imaging buried roots.

The backscatter system developed at University of Florida (UF) is based on Compton backscatter imaging (CBI) technique in which the radiation source and the detector are located on the same side of the target, as illustrated in Fig. 1. This application is useful when placing the detection plane on the opposite side of the X-ray source from the target is impossible or impractical. Therefore, CBI is a valuable non-destructive examination (NDE) tool because of its single-sided nature, penetrating abilities of radiation, and unique interaction properties of radiation with matter. Changes in the backscatter photon intensity are caused by differences in absorption and scattering cross-sections along the path of the scattered photons.

The novel backscatter technique uses an X-ray pencil or fan beam to illuminate the target while scintillation detectors positioned around the X-ray source count backscattered photons. A collimator (lead sleeve) placed around the detector ensures that photons scattered from

above the collimation plane are rejected while the detector records those that scatter from below. As the X-ray beam scans the target, a 2D image is created based on the recorded counts from each detector. Inherent in traditional pencil beam source is a trade-off between image resolution and acquisition time, higher resolution images typically requiring longer acquisition times. Fan beams offer more X-rays per unit time than traditional pencil beam sources; however, the fan beam cannot be used as a direct replacement for a pencil beam in a conventional system without leading to degraded image resolution. For in-field applications, to reduce the acquisition time significantly and to enable larger-scale field studies, fan beam geometry is preferred. However, for the lab setting both pencil and fan beam geometries are used to study the limitations and constraints in the current application.

The X-ray tube in the backscatter imaging system is a 450 KeV industrial X-ray tube (MXR-451HP/11) from COMET. The X-ray tube comes with a 5 mm thick inherent Beryllium filter. This imaging system uses four 2" x 2" cylindrical NaI(Tl) detectors for pencil beam geometry and GOS (gadolinium oxysulfide) or CsI(Tl) (Thallium activated Cesium Iodide) linear array detector for fan beam geometry. The field system developed can move at variable scanning speeds ranging from 1 to 40 inches/min.

This backscatter X-ray imaging technique has been used as a valuable tool in a number of applications in industry, medicine and national security such as railroad tie inspection, space shuttle foam inspection, and for detection of buried landmines.

Super Resolution Model

Training a SR model for backscatter X-ray images of plant roots is challenging since we do not have examples of LR-HR pairs. Therefore, in this effort, we apply a transfer learning approach that consists of training the SR model with images from alternative datasets. Figure 2 shows the deep-learning architectures that we use for SR (FSRCNN and SRGAN) and segmentation (SegRoot), and the training datasets used in each case. We use the segmentation network SegRoot for evaluation purposes only.

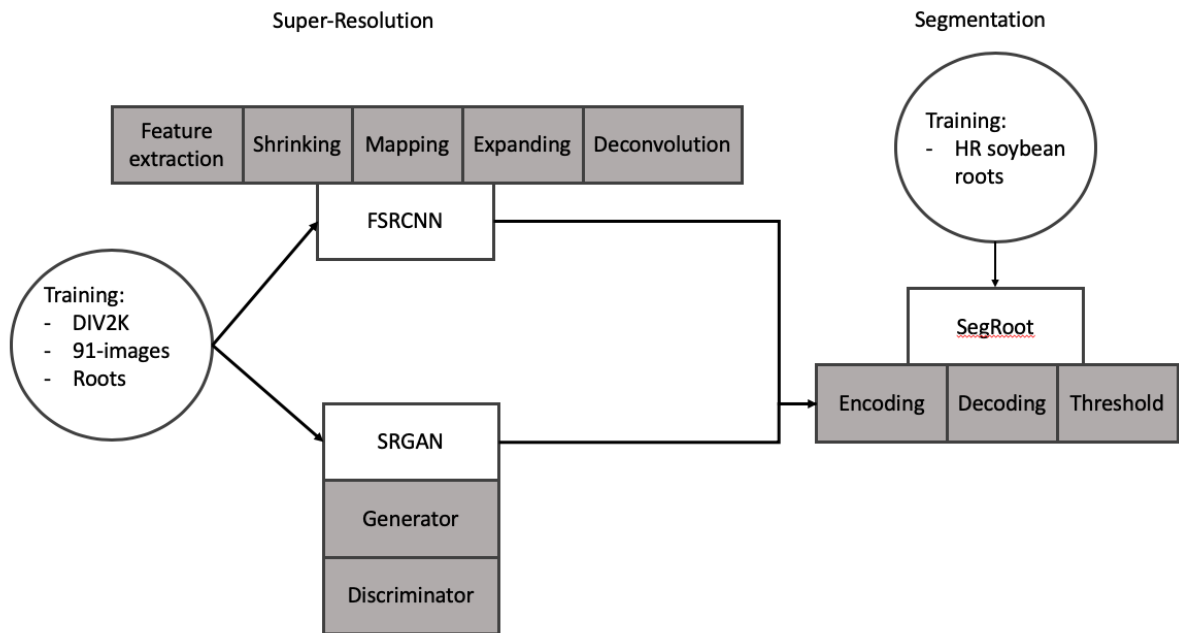


Figure 2. Left: Components of the SR network FSRCNN. Right: Components of the segmentation network SegRoot.

To map LR images into SR images, a vast amount of CNN architectures can be found in the literature. FSRCNN is an architecture that exhibits similar performance to state-of-the-art SR models but its execution is considerably faster. This is an advantage to compare different training datasets. FSRCNN is divided into five parts:

1. Feature extraction: FSRCNN consists of a convolutional layer with d filters of size 5×5 and 1 input channel. In this case, d is considered as the LR dimension. This part is denoted by $Conv(5, d, 1)$.
2. Shrinking: The purpose of a shrinking layer is reducing the LR dimension. The shrinking procedure is carried out by a convolutional layer of s 1×1 -filters, denoted by $Conv(1, s, d)$ where s is smaller than the number of input channels d .
3. Mapping: The mapping layer is a non-linear mapping that aims at estimating a shrunken version of the HR dimension. This layer is implemented as a sequence of m 3×3 convolutional layers. The number of filters is s for each layer. This mapping is denoted by $mxConv(3, s, s)$.

4. Expanding: The expanding layer is implemented using a number d of SR feature maps are estimated by a 1×1 convolutional layer (denoted by $Conv(1,d,s)$).
5. Deconvolution: The deconvolution component corresponds to a 9×9 deconvolution layer with 1 filter that upscales n times the height-and-width input dimensions. The deconvolution components denoted by $DeConv(9,1,d)$.

As suggested by the authors of FSRCNN, we apply a Parametric Rectified Linear Unit (PReLU) after each convolutional layer. Also, we set the parameters d , s , and m as 56, 12, and 4, respectively. It has been experimentally demonstrated that these values are suitable for recovering HR details.

Adversarial Networks

A generative adversarial network (GAN) is a machine learning system formed by two blocks, a generator G and a discriminator D , as illustrated in Fig. 1. In this configuration G and D play contrary roles, i.e., on the one hand, G aims at generating "realistic-like fake data" capable of fooling D , whereas D is continuously trained to classify fake data from real data (Goodfellow et al. 2014). Mathematically, the adversarial setting is formulated as follows

$$\min_G \max_D \mathbb{E}_{x \sim p(x)} \log(D(x)) + \mathbb{E}_{x \sim q(x)} \log(1 - D(G(x))) \quad (1)$$

where x denotes a sample (e.g., an image), and p and q are data distributions (e.g., distributions of LR and HR images). Since this is a min-max problem, the expression in (1) is both, a loss function and a reward function. The optimization problem is solved in an alternating manner. In one step, the loss function is minimized w.r.t. G , such that the output of $G(x)|_{x \sim p(x)}$ is optimized when $D(G(x))$ equals to 1. On the other hand, the expression in (1) is seen as a reward function that is maximized w.r.t. D . In this case, $D(x)$ is a classifier that is trained to output one when $x \sim p(x)$, and zero when $x \sim q(x)$.

In a SRGAN, $x \sim p(x)$ is a sample of a set of LR images, and $x \sim q(x)$ is a sample of a set of HR images. After several iterations, it is expected that the D is not able to tell apart HR and

SR images, i.e., G learns to convert LR images into SR images very similar to the original HR images. Note that in (1), it is not required that the output of the generator matches the HR version of the LR input, i.e., the content of the generated image might not be the same as the one in the LR one. To enforce the matching between HR-LR pairs, we add the squared error between the HR and SR images to the function as follows

$$\min_G \max_D \mathbb{E}_{x,y \sim p(x,y)} \log(D(x)) + \log(1 - D(G(y))) + \|x - G(y)\|^2 \quad (2)$$

where $x,y \sim p(x,y)$ is a pair of HR (x) and LR (y) images randomly sampled from a set of HR-LR image pairs, and $\|\cdot\|$ denotes the Euclidean norm. Note that in (2), when minimizing w.r.t. G , two terms are considered, $\log(1 - D(G(y)))$ and $\|x - G(y)\|^2$, which correspond to the generative adversarial loss and content loss, respectively (Ledig et al. 2017).

We modify the approach described in (2) by incorporating multiple D_i discriminators in the SRGAN architecture (one discriminator per dataset). Therefore, each discriminator acts as an expert to distinguish HR-SR images on one type of data. The optimization problem is written as follows

$$\min_G \max_D \sum_I \mathbb{E}_{x,y \sim p_i(x,y)} \log(D_i(x)) + \log(1 - D_i(G(y))) + \|x - G(y)\| \quad (3)$$

where D_i is the discriminator specialized in the i -th dataset. We hypothesize that in this way the generator will output more general SR images since it is more challenging to “cheat” several specialized discriminators (one per type of data) than a general one (a discriminator that distinguishes HR vs. SR images of any kind).

To choose the architecture of D and G , we need a two-class classification network, and a network that outputs a matrix of the same size of the input (since the LR image is interpolated to the size of the desired SR image), respectively. We evaluated several architectures and selected two for their balance between performance and computational requirements. As a G network, we use the convolutional super-resolution layers of the resolution-aware convolutional neural network (RACNN) proposed in (Cai et al. 2019). For D , we design a two-class classifier with three convolutional layers and one fully-connected layer.

For training, we use a batch size of 100, and as an update rule, we apply Adaptive Moment Estimation (Adam), applied also in the method proposed by (Ledig et al. 2017), with a learning rate of 0.001. To create LR training images, we randomly select 64×64 chunks, downsample them to 16×16 size and upsample them again to the original size by bicubic interpolation.

SR Evaluation

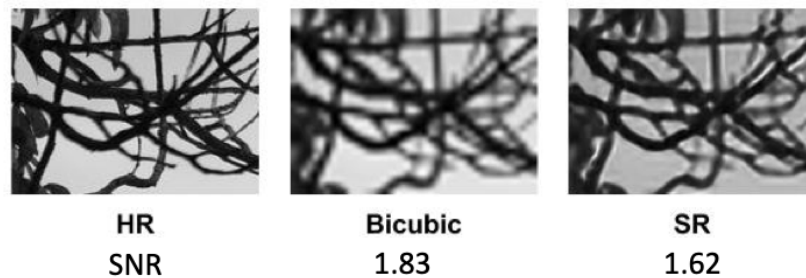


Figure 3. The SNR and the perceptual quality of an image are not always directly correlated.

We quantitatively evaluate the SR performance by two measures: SNR and IoU. SNR is a classic measure for estimating the quality of a recovered signal. It is computed by a pixel-by-pixel comparison between the original HR image and the estimated SR image, as follows

$$SNR = 10 \log \log \frac{1}{\|HR-SR\|^2}.$$

However, SNR might not necessarily highlight any HR detail enhancement. For example, in Fig. 3, the SNR (the higher the better) of the image estimated by bicubic interpolation (1.83) is higher than the SNR of the SR image (1.62) ---even though the interpolated image looks blurred. For this reason, we also estimate the effect of applying the SR enhancement as a preprocessing step in an automatic root to background segmentation process. To this end, we train the state-of-the-art SegRoot network (Wang et al. 2019) with HR data. Therefore, we assume that the segmentation would be more accurate if the input data contains HR details as the ones used for training. We compare the binary ('1'-pixels indicate root, and '0'-pixels indicate background) segmented images B_{seg} with manually

labeled images B_{gt} by the IoU (Rahman and Wang 2016), also known as the Jaccard Index computed by

$$IoU = \frac{|B_{seg} \cdot B_{gt}|}{|B_{seg}| + |B_{gt}|}$$

where ' $| \cdot |$ ' denotes the sum of all the entries of the input matrix and ' \cdot ' is a pointwise multiplication. The IoU values are between 0 and 1 (the higher the better). IoU is '1' when all the target pixels are correctly classified and there is not false positives.

Datasets

In this study, we use two five datasets (two non-plant root datasets and three plant-root datasets) to train the SR models. They are listed below:

- DIV2K (<https://data.vision.ee.ethz.ch/cvl/DIV2K/>): a dataset of natural images that has been used by others to train and test SR algorithms. We train our models on the grayscale version of the training dataset (800 images).
- 91-Image (<https://www.kaggle.com/ll01dm/t91-image-dataset>): a classical dataset commonly used in SR studies.
- Arabidopsis thaliana roots (<https://zenodo.org/record/50831#.XjIAPVNKhQI>): an Arabidopsis thaliana dataset for root phenotyping analysis (Bouché et al. 2016).
- Wheat roots (<http://gigadb.org/dataset/100346>): a data set consisting of 2614 images of wheat seedlings (Atkinson et al. 2017).
- Barley roots: a set of 3-D magnetic resonance images (MRI) of barley roots (<https://www.plant-image-analysis.org/dataset/3d-magnetic-resonance-images-of-barley-roots>). This dataset also contains WinRHIZO images of the barley roots.

In our experiments, we group the three plant-root datasets (Arabidopsis thaliana, Wheat and Barley) into one that we call "Roots". RGB images were converted to grayscale.

To test the performance of the SR models, we use two datasets:

- Soybean roots (<https://github.com/wtwtw0330/SegRoot>): a data set consisting of 65 images of soybean roots (Wang et al. 2019).

- Backscatter X-ray images: data set consisting of our backscatter X-ray system to acquire images of pieces of roots and root vegetables (a sweet potato, radish, and cassava) buried in a potting soil mix.

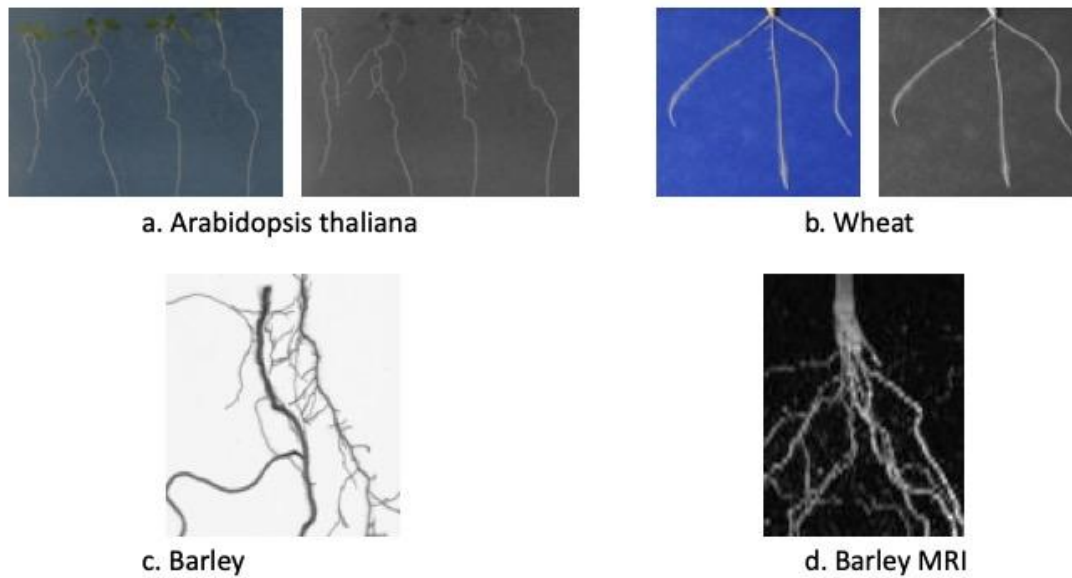


Figure 4. Examples of plant-root images used to train SR models. RGB images of *Arabidopsis thaliana* roots (a) and wheat roots (b) were converted to grayscale.

Figure 4 shows examples of the plant-root datasets used for training the SR model.

RESULTS

We trained nine SR models:

- FSRCNN-DIV2K: FSRCNN trained with the DIV2K dataset.
- FSRCNN-91-image: FSRCNN trained with the 91-image dataset.
- FSRCNN-non-roots&roots: FSRCNN-91-image model fined tuned with the DIV2K and Roots datasets.
- SRGAN-DIV2K: SRGAN trained with the DIV2K dataset.
- SRGAN-91-image: SRGAN trained with the 91-image dataset.
- SRGAN-non-roots&roots: SRGAN-91-image model fined tuned with the DIV2K and Roots datasets.

- SRGAN-MULDIS: SRGAN model trained with three discriminators (one for each dataset: DIV2K, 91-image and Roots).

For all the SR training experiments, we use as validation dataset a subset of the 100 images from the Roots dataset. The validation dataset is used to estimate the performance of the model in terms of the SNR after completing each iteration. After finishing the training process, we take as the parameters of the model the ones that output the highest SNR on the validation test. Each model is trained 100 iterations (we noticed that by this value the loss function converges).

All the computational experiments were performed in a Linux Centos 7 machine, x86_64, Intel Xeon CPU @3.60 GHz with a GPU GeForce RTX. For implementation, we used the deep learning framework PyTorch 1.2.0.

To evaluate the performance of the SR models, we downscale the grayscale images of the Soybean dataset by four. We use one of the SR models listed above to upscale the test images to their original resolution. We estimate the SNR by comparing the estimated SR images and original HR images. Afterward, we use the SegRoot network to classify each pixel in the input image as root or non-root. As lower and upper bounds, we take the upscaled images by bicubic interpolation, and the original HR images, respectively. Note that the bicubic interpolation is an upscaling method that does not require training. Table 1 contains the SNR and IoU obtained on the grayscale-Soybean dataset. These results show that all the SR models outperform the bicubic interpolation in terms of both SNR and IoU. Regarding only the SR models, FSRCNN-91-image, FSRCNN-roots, and SRGAN-MULDIS exhibit the highest SNR (we consider that there is not statistical evidence to prefer one of them in this case since their standard error overlaps). However, there is a mismatch between SNR and IoU results. The model that performs the best in terms of the IoU is FSRCNN-91-image&roots. Therefore, the features enhanced by the SR models that allows increasing the SNR do not necessarily imply that can be useful for any task, as the applied automatic segmentation. Figure 5 contains examples of SR and segmented.

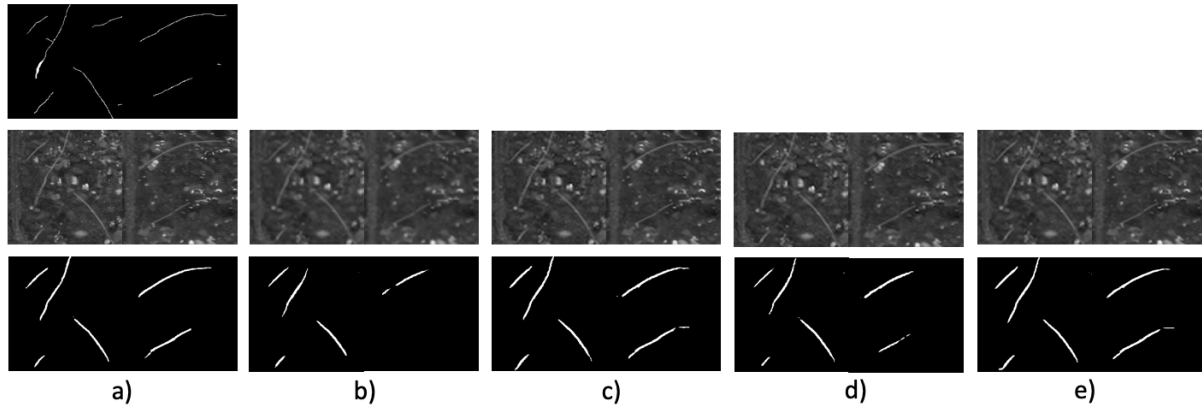


Figure 5. SR and segmentation example images (128x64) on the soybean dataset. From top to bottom: a) ground-truth, HR image and segmentation on HR image; b) Bicubic image and its segmentation; c) FSRCNN-91-image model and its segmentation; d) SRGAN-MULDIS model and its segmentation; and e) FSRCNN-91-image&roots model and its segmentation.

Table 1. Evaluation of SR models on Soybean dataset. SNR and IoU mean (and standard error in parentheses)

Model	SNR	IoU
1. Bicubic	28.30 (1.37)	0.0984 (0.0098)
2. FSRCNN-DIV2K	32.60 (0.19)	0.1313 (0.0106)
3. FSRCNN-91-image	33.10 (0.20)	0.1419 (0.0108)
4. FSRCNN-roots	33.05 (0.20)	0.1623 (0.0111)
5. FSRCNN -91-image&roots	32.48 (0.19)	0.1709 (0.0110)
6. SRGAN-DIV2K	32.48 (0.19)	0.1402 (0.0106)
7. SRGAN-91-image	32.47 (0.19)	0.1327 (0.0107)
8. SRGAN-roots	32.71 (0.19)	0.1485 (0.0108)
9. SRGAN-91-image&roots	32.66 (0.20)	0.1536 (0.0108)
10. SRGAN-MULDIS	33.05 (0.20)	0.1415 (0.0108)
11. HR	---	0.2003 (0.0122)

For further analysis on the segmentation experiments, we randomly select 200 64x64 chunks from the Soybean dataset and carry out a pairwise comparison by counting the number of times that one model outperforms other. These results show that the segmentation

is better when using FSRCNN-91-image&roots for most images than when using any of the other studied SR models or bicubic interpolation. Also, the segmentation carried out on HR always exhibits better performance. We infer that the HR details on the images boost the performance of the SegRoot model on this data.

Table 2. Pairwise IoU comparison of SR models. The value on the left indicates the number of chunks where the left model outperforms the top model. The value on the right indicates the number of images for which the IoU is the same for both models (usually when the IoU is 0). The numeration of the models 1-11 is the same as in Table 1.

	1.	2.	3.	4.	5.	6.	7.	8.	9.	10.	11.
1.	0 200	28 64	37 49	27 39	2 38	22 54	37 59	68 18	28 43	41 48	40 33
2.	108 64	0 200	66 48	46 40	44 38	66 50	69 55	82 15	61 41	63 46	50 30
3.	114 49	86 48	0 200	37 38	35 35	75 45	95 50	92 12	56 40	75 45	43 32
4.	134 39	114 40	125 38	0 200	55 36	110 37	122 41	106 8	93 35	105 40	60 26
5.	138 38	118 38	130 35	9 36	0 200	124 36	128 40	110 10	108 38	124 40	61 29
6.	124 54	84 50	80 45	53 37	40 36	0 200	82 52	90 12	57 42	69 45	50 29
7.	104 59	76 55	55 50	37 41	32 40	66 52	0 200	84 15	42 44	54 50	43 32
8.	114 18	103 15	96 12	86 8	80 10	98 12	101 15	0 200	92 10	94 14	75 200
9.	129 43	98 41	104 40	72 35	54 38	101 42	114 44	98 10	0 200	101 44	56 29
10.	111 48	91 46	80 45	55 40	36 40	86 45	96 50	92 14	55 44	0 200	44 33
11.	127 33	120 30	125 32	114 26	110 29	121 29	125 32	113 12	115 29	123 33	0 200

Backscatter X-Ray Images

We apply FSRCNN-roots ---since it exhibits an appropriate balance between SNR and IoU performance in the previous experiments--- to X-ray backscatter images of pieces of buried roots.

This SR model allows increasing four times the resolution of the original backscatter X-ray images. To illustrate the resolution, in Fig. 6, we put each image together with the same image overlapped with a 1cm x 1cm-cell grid. The images correspond to buried vegetables (sweet potato, radish, and cassava) at 5-inch depth in potting mix soil and vermiculite, and pieces of tree roots packed in a soil core filled in with potting mix soil.

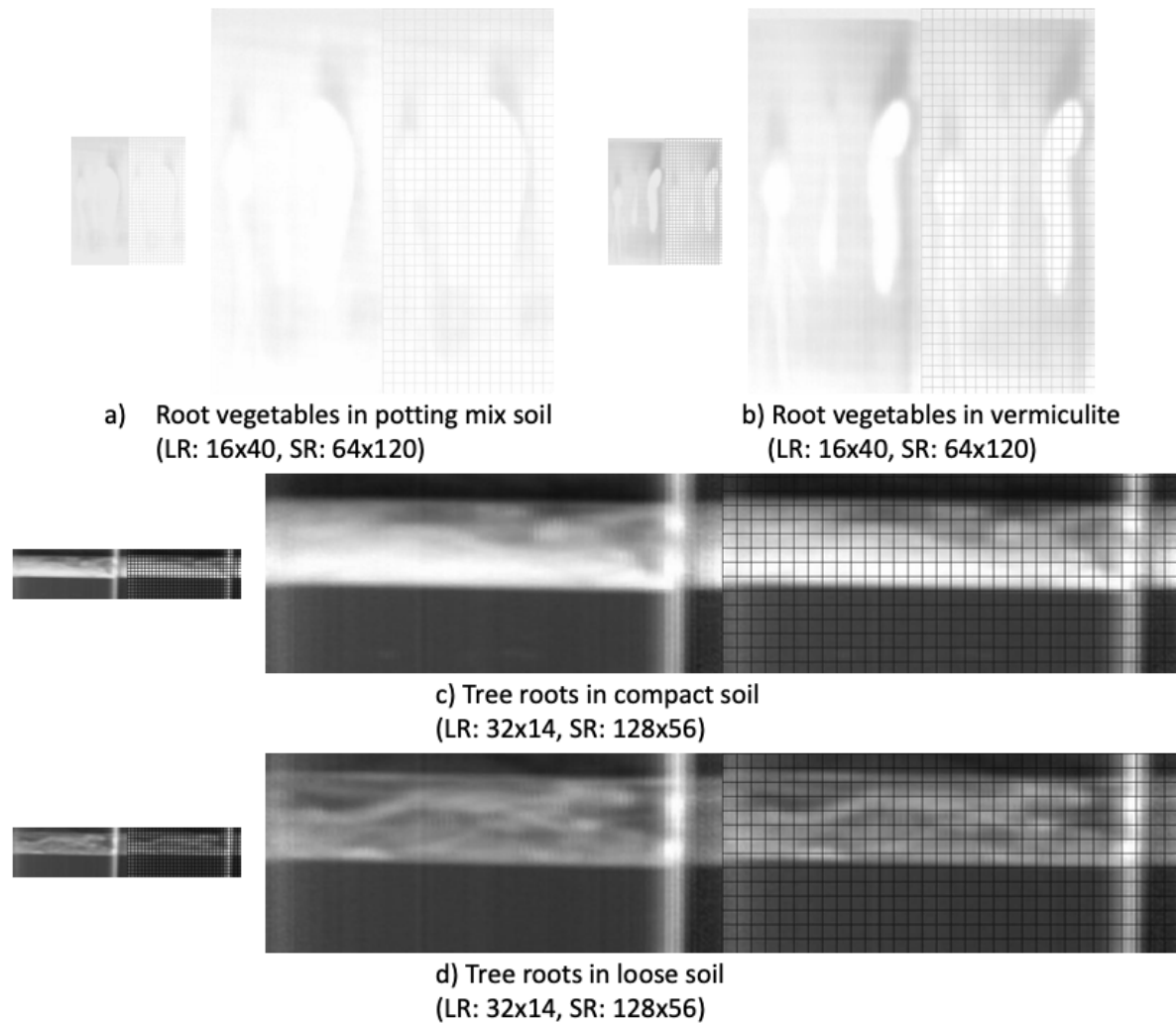


Figure 6. Original backscatter X-ray images (small) and SR images (large) increased four times the original size (each cell on the grid is 1cm x 1cm). The top images correspond to buried root vegetables (sweet potato - left, radish - middle, and cassava - right) at 5-inch depth.

DISCUSSION

The current technology for non-intrusive root imaging often acquires noisy and low-resolution images. In this study, we show that this issue can be tackled by incorporating the use of a SR model in the image formation process. We design a framework for the application of deep-learning based SR models to recover HR details on images of roots lost in the acquisition process.

One of the challenges for implementing an appropriate SR algorithm for root imaging with X-ray backscatter technology is that there are no HR images of this type to train the model. To overcome this, we proposed training the SR model using a variety of data types.

We demonstrate that the SR models outperforms the basic bicubic interpolation even when trained with non-root datasets. Also, our segmentation experiments show that a high performance on this task can be achieved independently of the SNR. Therefore, we conclude that the quality of the image enhancement depends on the application.

We apply SR on buried images acquired by a backscatter X-ray system. We show that increasing 4 times the size of the images facilitates the visual inspection of the images and the generation of ground-truth for training segmentation and feature extraction models.

In addition to SR, the pipeline of image processing might include other stages that deal with artifacts in the images, such as denoising and contrast enhancement. To incorporate any new stage, we recommend using the two-section evaluation method that we applied on this paper: evaluation of the performance directly on the processed image, and evaluation of the result when performing a machine learning task on the processed image. Also, we suggest using SR models for improving the performance of other machine learning tasks such as feature extraction and classification.

Future work could include combining FSRCNN and SRGAN by using the discriminator and loss function of SRGAN and the generator of FSRNN. In this work, we generate LR samples by downscaling the original HR images. Therefore, an extension of this work might consider using an alternative to transform HR into LR images, such as “blind SR kernel estimation” methods.

ACKNOWLEDGMENTS

This work was funded by the Advanced Research Projects Agency-Energy (ARPA-E) under Award Number P0056459. The views and opinions of authors expressed herein do not necessarily state or reflect those of the United States Government or any agency thereof.

REFERENCES

- Araus, J.L. and Cairns, J.E. 2014. Field high-throughput phenotyping: the new crop breeding frontier. *Trends in Plant Science* 19(1), pp. 52–61.
- Atkinson, J.A., Lobet, G., Noll, M., Meyer, P.E., Griffiths, M. and Wells, D.M. 2017.

- Combining semi-automated image analysis techniques with machine learning algorithms to accelerate large-scale genetic studies. *GigaScience* 6(10), pp. 1–7.
- Atkinson, J.A., Pound, M.P., Bennett, M.J. and Wells, D.M. 2019. Uncovering the hidden half of plants using new advances in root phenotyping. *Current Opinion in Biotechnology* 55, pp. 1–8.
- Barton, C.V.M. and Montagu, K.D. 2004. Detection of tree roots and determination of root diameters by ground penetrating radar under optimal conditions. *Tree Physiology* 24(12), pp. 1323–1331.
- Blau, Y., Mechrez, R., Timofte, R., Michaeli, T. and Zelnik-Manor, L. 2019. The 2018 PIRM Challenge on Perceptual Image Super-Resolution. In: Leal-Taixé, L. and Roth, S. eds. *Computer Vision – ECCV 2018 Workshops: Munich, Germany, September 8-14, 2018, Proceedings, Part V*. Lecture notes in computer science. Cham: Springer International Publishing, pp. 334–355.
- Bouché, F., D'Aloia, M., Tocquin, P., Lobet, G., Detry, N. and Périlleux, C. 2016. Root Phenotyping Data. *Zenodo*.
- Cai, D., Chen, K., Qian, Y. and Kämäräinen, J.-K. 2019. Convolutional low-resolution fine-grained classification. *Pattern recognition letters* 119, pp. 166–171.
- Cao, Y., Repo, T., Silvennoinen, R., Lehto, T. and Pelkonen, P. 2011. Analysis of the willow root system by electrical impedance spectroscopy. *Journal of Experimental Botany* 62(1), pp. 351–358.
- Clark, R.T., MacCurdy, R.B., Jung, J.K., et al. 2011. Three-dimensional root phenotyping with a novel imaging and software platform. *Plant Physiology* 156(2), pp. 455–465.
- Cseresnyés, I., Szitár, K., Rajkai, K., et al. 2018. Application of Electrical Capacitance Method for Prediction of Plant Root Mass and Activity in Field-Grown Crops. *Frontiers in plant science* 9, p. 93.
- Cui, S., Nimmagadda, J.K. and Baciak, J.E. 2017. Backscatter Radiography as a Non-Destructive Examination Tool for Concrete Structures. In: *2017 IEEE Nuclear Science Symposium and Medical Imaging Conference (NSS/MIC)*. IEEE, pp. 1–6.
- Dalton, F.N. 1995. In-situ root extent measurements by electrical capacitance methods. *Plant and soil* 173(1), pp. 157–165.
- Das Choudhury, S., Samal, A. and Awada, T. 2019. Leveraging Image Analysis for High-Throughput Plant Phenotyping. *Frontiers in plant science* 10, p. 508.
- Dong, C., Loy, C.C. and Tang, X. 2016. Accelerating the Super-Resolution Convolutional Neural Network. In: Leibe, B., Matas, J., Sebe, N., and Welling, M. eds. *Computer vision – ECCV 2016*. Lecture notes in computer science. Cham: Springer International Publishing, pp. 391–407.
- Endler, T.M.J.A. 1998. The Relative Success of Some Methods for Measuring and Describing the Shape of Complex Objects. *Systematic Biology* 47(2), pp. 264–281.
- Goodfellow, I., Pouget-Abadie, J., Mirza, M., et al. 2014. Generative Adversarial Nets.
- Green, W.A., Little, S.A., Price, C.A., et al. 2014. Reading the leaves: A comparison of leaf rank and automated areole measurement for quantifying aspects of leaf venation. *Applications in plant sciences* 2(8).
- Han, J.G., Cao, H., Barb, A., Punyasena, S.W., Jaramillo, C. and Shyu, C.-R. 2014. A Neotropical Miocene Pollen Database Employing Image-Based Search and Semantic Modeling. *Applications in plant sciences* 2(8), p. 1400030.
- Hirano, Y., Dannoura, M., Aono, K., et al. 2009. Limiting factors in the detection of tree roots using ground-penetrating radar. *Plant and soil* 319(1–2), pp. 15–24.
- Johnson, M.G., Tingey, D.T., Phillips, D.L. and Storm, M.J. 2001. Advancing fine root

- research with minirhizotrons. *Environmental and experimental botany* 45(3), pp. 263–289.
- Kolb, E., Legué, V. and Bogeat-Triboulot, M.-B. 2017. Physical root-soil interactions. *Physical Biology* 14(6), p. 065004.
- Krieger, J.D. 2014. A protocol for the creation of useful geometric shape metrics illustrated with a newly derived geometric measure of leaf circularity. *Applications in plant sciences* 2(8).
- Ledig, C., Theis, L., Huszar, F., et al. 2017. Photo-Realistic Single Image Super-Resolution Using a Generative Adversarial Network. In: *2017 IEEE Conference on Computer Vision and Pattern Recognition (CVPR)*. IEEE, pp. 105–114.
- Majdi, H. 1996. Root sampling methods - applications and limitations of the minirhizotron technique. *Plant and soil* 185(2), pp. 255–258.
- Pflugfelder, D., Metzner, R., van Dusschoten, D., Reichel, R., Jahnke, S. and Koller, R. 2017. Non-invasive imaging of plant roots in different soils using magnetic resonance imaging (MRI). *Plant Methods* 13, p. 102.
- Rahman, M.A. and Wang, Y. 2016. Optimizing Intersection-Over-Union in Deep Neural Networks for Image Segmentation. In: Bebis, G., Boyle, R., Parvin, B., et al. eds. *Advances in visual computing*. Lecture notes in computer science. Cham: Springer International Publishing, pp. 234–244.
- Tabb, A., Duncan, K.E. and Topp, C.N. 2018. Segmenting Root Systems in X-Ray Computed Tomography Images Using Level Sets. In: *2018 IEEE Winter Conference on Applications of Computer Vision (WACV)*. IEEE, pp. 586–595.
- Taylor, H.M., Upchurch, D.R. and McMichael, B.L. 1990. Applications and limitations of rhizotrons and minirhizotrons for root studies. *Plant and soil* 129(1), pp. 29–35.
- Trachsel, S., Kaepler, S.M., Brown, K.M. and Lynch, J.P. 2011. Shovelomics: high throughput phenotyping of maize (*Zea mays* L.) root architecture in the field. *Plant and soil* 341(1–2), pp. 75–87.
- Wang, T., Rostamza, M., Song, Z., et al. 2019. SegRoot: A high throughput segmentation method for root image analysis. *Computers and Electronics in Agriculture* 162, pp. 845–854.
- Wang, Z., Liu, D., Yang, J., Han, W. and Huang, T. 2015. Deep Networks for Image Super-Resolution with Sparse Prior. In: *2015 IEEE International Conference on Computer Vision (ICCV)*. IEEE, pp. 370–378.
- Wu, Q., Wu, J., Zheng, B. and Guo, Y. 2018. Optimizing soil-coring strategies to quantify root-length-density distribution in field-grown maize: virtual coring trials using 3-D root architecture models. *Annals of Botany* 121(5), pp. 809–819.
- Yang, J., Wright, J., Huang, T.S. and Ma, Y. 2010. Image super-resolution via sparse representation. *IEEE transactions on image processing : a publication of the IEEE Signal Processing Society* 19(11), pp. 2861–2873.
- Zeyde, R., Elad, M. and Protter, M. 2012. On Single Image Scale-Up Using Sparse-Representations. In: Boissonnat, J.-D., Chenin, P., Cohen, A., et al. eds. *Curves and Surfaces*. Lecture notes in computer science. Berlin, Heidelberg: Springer Berlin Heidelberg, pp. 711–730.
- Zhang, H., Zhang, Y., Li, H. and Huang, T.S. 2012. Generative bayesian image super resolution with natural image prior. *IEEE Transactions on Image Processing* 21(9), pp. 4054–4067.
- Zhang, Y. and An, M. 2017. Deep Learning- and Transfer Learning-Based Super Resolution Reconstruction from Single Medical Image. *Journal of healthcare engineering* 2017, p. 5859727.